Journal of Physics D:
Applied Physics

PAPER • **OPEN ACCESS**

Applying stochastic Langevin function with coupled Brownian–Néel relaxations to study the dynamic magnetizations of nanoparticle tracers in magnetic particle imaging

To cite this article: Ebrahim Azizi *et al* 2025 *J. Phys. D: Appl. Phys.* **58** 135002

OPEN ACCESS
IOP Publishing
Journal of Physics D: Applied Physics
J. Phys. D: Appl. Phys. **58** (2025) 135002 (10pp)
https://doi.org/10.1088/1361-6463/adafbd

Applying stochastic Langevin function with coupled Brownian–Néel relaxations to study the dynamic magnetizations of nanoparticle tracers in magnetic particle imaging

Ebrahim Azizi[1], Shahriar Mostufa[1], Bahareh Rezaei[1], Shumin Xin[2], Jiajia Sun[2], Zongqian Shi[2], Jenifer Gómez-Pastora[3] and Kai Wu[1,*]

[1] Department of Electrical and Computer Engineering, Texas Tech University, Lubbock, TX 79409, United States of America
[2] State Key Laboratory of Electrical Insulation and Power Equipment, Xi'an Jiaotong University, No. 28 Xianning West Road, Xi'an, Shaanxi Province 710049, People's Republic of China
[3] Department of Chemical Engineering, Texas Tech University, Lubbock, TX 79409, United States of America

E-mail: kai.wu@ttu.edu

Received 7 August 2024, revised 20 January 2025
Accepted for publication 29 January 2025
Published 6 February 2025

Abstract

Magnetic particle imaging (MPI) is a new imaging technique that utilizes biologically safe iron oxide nanoparticle tracers for medical imaging. Although in the preclinical stage, MPI has shown strong potential for applications such as cell tracking, angiography, cancer imaging, etc. With the ever-growing research interest in MPI and the increasing desire to apply it in clinical medical imaging, the design of tracers, MPI systems, image reconstruction algorithms, and other related components has become increasingly critical. To date, most of the theoretical studies in MPI rely on the static Langevin function to describe the magnetization responses of superparamagnetic iron oxide nanoparticle (SPION) tracers. However, under a fast-changing excitation field (usually tens of kHz), the magnetic relaxation time of SPION tracers is no longer negligible, thus, the static Langevin function is inaccurate in explaining the tracers' magnetic signals in MPI. Herein, we apply a stochastic Langevin function with coupled Brownian–Néel relaxation models to study the dynamic magnetization responses of SPION tracers in MPI. The time domain magnetization responses (M–t curve), dynamic magnetization-field hysteresis loops (M–H curve), and point spread functions are modeled for different SPION tracer designs with varying physical and magnetic properties. Our results show that larger magnetic core sizes

* Author to whom any correspondence should be addressed.

reduce the MPI spatial resolution. Conversely, thicker non-magnetic coatings on tracers do not significantly affect the spatial resolution. The increased anisotropy diminishes the MPI resolution, and a higher saturation magnetization favors higher MPI resolution.

Keywords: magnetic particle imaging, magnetic nanoparticle, stochastic Langevin function, point spread function, dynamic magnetization response

1. Introduction

Magnetic particle imaging (MPI) is an emerging imaging modality that directly images the spatial distribution of superparamagnetic iron oxide nanoparticle (SPION) tracers, offering outstanding contrast and sensitivity [1–3]. Due to the paramagnetic and diamagnetic nature of biological tissues, MPI has zero background noise and its signal is linearly and quantitatively proportional to the tracers. To date, MPI has been exploited in various imaging applications such as cell tracking [4], functional brain imaging [5, 6], gastrointestinal bleeding imaging [7], etc. Numerous recent studies have focused on exploring the fundamental parameters of MPI to enhance and optimize its imaging outcomes. For example, Yoshida and Enpuku investigated the field-dependent Néel relaxation time, one of the critical factors in MPI [8]. Their study elucidated the transitions between Néel-dominant and Brownian-dominant regimes under the influence of the excitation field. Feng *et al* developed a multi-exponential relaxation spectral analysis method to quantify Néel and Brownian relaxation times in the magnetization recovery process of pulsed vascular MPI [9]. Their approach demonstrates the potential for multi-contrast vascular imaging.

In MPI, a homogeneous sinusoidal magnetic field, namely, the excitation field, is applied to trigger the nonlinear magnetic responses of SPION tracers, which are recorded by a pair of receive coils. A field-free region (FFR) created by a gradient field is applied to localize the signal, where only the SPION tracers that are in the FFR can respond to the excitation field and generate a signal. Whereas tracers outside the FFR are magnetically 'fixed' or fully saturated by the non-zero gradient field, and their magnetic responses are almost constant over time. The MPI tomographic scanning is achieved by rastering this FFR through the field of view following a pre-defined scanning trajectory. Thus, the magnetic signals recorded by the receive coils are assigned to a spatial location correlated to the instantaneous location of the FFR. Nowadays, there are two popular methods for MPI image reconstruction, namely, the frequency-space (f-space) [10, 11] that exploits system function and harmonics of tracers and the real-space (x-space) [12–14] that relies on the real-time voltage signals generated by the flipping of tracers' magnetizations in FFR. Both imaging strategies benefit from SPION tracers that show narrow and steep magnetic responses. The current MPI imaging resolution is sub-1 mm and could potentially be improved to sub-300 μm with an optimized tracer, field, and image-reconstruction algorithm design [15, 16].

The f-space MPI image reconstruction requires an accurate system matrix, the traditional calibration method for building the system matrix is time-consuming and could introduce noise during the delta sample calibration process, furthermore, it suffers from limited generalizability and spatial resolution. Researchers have proposed a model-based method for building the system matrix, which is faster and can be easily modified to fit different MPI systems and different tracers [11, 17, 18]. However, the model-based method suffers from the inaccuracy of modeling the magnetization behaviors of SPION tracers in fluids. A more reliable model that can describe the magnetization dynamics of the tracers has a significant impact on improving the resolution in both f-space and x-space MPI image reconstruction. For example, Kluth *et al* replaced the Langevin function with a Fokker–Planck equation in the f-space multi-dimensional MPI imaging, joining the effort to improve imaging accuracy [18]. Li *et al* replaced the Langevin function with a modified Jiles–Atherton model, considering the relaxation effect of tracers, and improved the x-space MPI resolution [19].

For both f-space (Bruker) and x-space (Magnetic Insight) MPI, an ideal tracer response to the excitation field should behave like a delta function, corresponding to a step magnetization-field curve (M–H curve) that switches signs at zero field. Thus, a higher harmonic intensity (f-space) and voltage signal (x-space) can be recorded, favoring a higher signal-to-noise ratio (SNR) for image reconstruction. However, in reality, SPIONs show an 'S'-shape M–H curve under a slowly changing magnetic field, which can be fitted and described by the static Langevin function [20]. SPIONs often exhibit anisotropy due to combined magnetocrystalline, shape, and surface anisotropies. Assuming uniaxial anisotropy, where the magnetic moment aligns along a single easy axis, the particle's energy can be expressed through the joint anisotropy energy and Zeeman energy when subjected to an external field. The Stoner–Wohlfarth model shows that the hysteresis loop's width varies with the angle between the easy axis and the applied field. Although it accounts for anisotropy, the model assumes equilibrium conditions and does not consider thermal energy or particle relaxation [20]. The Brownian and Néel relaxations are two primary mechanisms by which SPIONs can rotate their magnetic moments when the equilibrium state is disrupted [21, 22]. Typically, the faster relaxation mechanism dominates, though both relaxation processes play a role in SPIONs' magnetization dynamics. In the linear response regime, where the applied field amplitude is much lower than the saturation field of nanoparticles and the frequency is high. The Debye model, which

uses complex magnetic susceptibility and effective relaxation time to account for the magnetization's phase delay to the field, is sufficient to describe the magnetization dynamics of SPIONs. However, in MPI, the high frequency and high amplitude of the excitation field (around 25 kHz, 10–20 mT/μ_0) cause non-equilibrium states and nonlinear magnetization responses in SPIONs, where the Brownian and Néel relaxation times become interdependent, influenced by particle size (core and hydrodynamic), temperature, and viscosity. Additionally, the relaxation time becomes dependent on the applied field, a factor previously overlooked, exceeding limits relevant to many biomedical applications [22, 23]. Therefore, model refinement must account for field-dependent relaxation times. To this end, the stochastic Langevin [24–27] and the Fokker–Planck [28] models are well-established approaches that address the field dependence of relaxation times, non-equilibrium, and nonlinearity, as observed in real MPI systems. As a result of the excitation field that is around tens of kHz, where the magnetization responses of SPIONs are no longer in an equilibrium state at any instantaneous time and their magnetization relaxations are no longer negligible and have field dependency. Thus, the traditional static Langevin function and Debye model are no longer valid for explaining the dynamic magnetization responses of SPIONs for MPI.

In this work, we consider the magnetizations of single-domain SPIONs at the micromagnetic level, where the magnetization is determined by the micromagnetic field [18]. To model the magnetization dynamics of an ensemble of 1000 SPIONs, we employ the Landau–Lifshitz–Gilbert (LLG) equation with the inclusion of thermal noise. The ensemble's magnetization is averaged at stochastic time intervals defined by the Wiener process. Furthermore, we account for the effects of Brownian motion on the magnetization dynamics of monodispersed SPIONs with varying sizes, saturation magnetization, and anisotropy values. To capture these effects, we consider the LLG model, Brownian motion, thermal field noise, and torque noise in a coupled system of stochastic differential equations, namely, the stochastic Langevin function [24–27]. This model considers the coupled Brownian and Néel relaxations to model the dynamic magnetizations of SPION tracers for MPI. By varying the physical and magnetic properties of SPION tracers, we modeled their time domain magnetization responses (M–t curve), dynamic magnetization-field hysteresis loops (M–H curve), and point spread functions (PSFs) under an excitation field. An ensemble of 1000 non-interacting SPIONs is assumed in the FFR that is only subjected to the excitation field. It has been reported that the intrinsic spatial resolution of MPI is correlated to the full width at half maximum (FWHM) of the PSF [29–32]. Thus, we also collected the FWHM values from the PSF as an indicator to evaluate the performance of tracers for achieving higher MPI spatial resolution.

2. Mathematical models

The magnetization dynamics of noninteracting, isotropic, and identical particles can be represented by the static Langevin function. However, the accuracy of this model depends on the equilibrium approximation. When the Néel and Brownian relaxation times are significant, the magnetization response is better described using the stochastic Langevin function considering the combined Néel-Brownian rotations [24–26]. This model accounts for the rotational dynamics of both the magnetic core of the particle and the entire particle which includes its core and coatings. Additionally, it incorporates the effects of Néel and Brownian relaxation times along with thermal noise influencing the rotation dynamics of both the magnetization and the particle's easy axis. In this framework, the overall torque applied to the easy axis **n** (see figure 1) evolves as described by equation (1), and the internal magnetization vector **m** (see figure 1), governed by the LLG equation in equation (2), is influenced by the effective field **H** in equation (3):

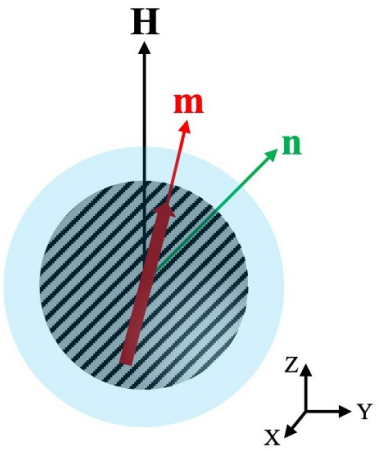

Figure 1. Schematic drawing of magnetic moment unit vector **m**, effective field **H**, and easy axis **n**, of a SPION tracer.

$$\frac{\mathrm{d}\boldsymbol{n}}{\mathrm{d}t} = \left(\frac{\boldsymbol{\theta}}{6\eta V_\mathrm{h}}\right) \times \boldsymbol{n} \tag{1}$$

$$\frac{\mathrm{d}\boldsymbol{m}}{\mathrm{d}t} = \frac{\gamma}{1+\alpha^2}\left(\boldsymbol{H} + \alpha \boldsymbol{m} \times \boldsymbol{H}\right) \times \boldsymbol{m} \tag{2}$$

where α is the damping coefficient, γ is the electron gyromagnetic ratio, η is the viscosity, V_h is the particle hydrodynamic volume expressed by $V_\mathrm{h} = \frac{\pi}{6} {D_\mathrm{h}}^3$ where D_h is the hydrodynamic diameter, and θ is the torque vector. The total particle energy describes the effective field and torque in equations (3) and (4). For an ensemble of non-interacting SPIONs where the dipole-dipole interactions are ignored, the effective field and torque can be written as the following equations:

$$\boldsymbol{H} = \boldsymbol{H}_{app} + \frac{2K_\mathrm{a}V_\mathrm{c}}{\mu}\left(\boldsymbol{m}\cdot\boldsymbol{n}\right)\boldsymbol{n} + \boldsymbol{H}_{th} \tag{3}$$

$$\theta = -2K_\mathrm{a}V_\mathrm{c}\left(\boldsymbol{m}\cdot\boldsymbol{n}\right)\left(\boldsymbol{m}\times\boldsymbol{n}\right) + \boldsymbol{\theta}_{th} \tag{4}$$

where K_a is the magnetic anisotropy constant, V_c is the magnetic core volume expressed by $V_\mathrm{c} = \frac{\pi}{6} {D_\mathrm{c}}^3$ where D_c is the magnetic core diameter, H_app is the externally applied magnetic field, μ is the magnitude of one SPION's magnetic

moment expressed by $\mu = V_c M_S$, where M_S is the saturation magnetization value of SPION, and $\boldsymbol{H_{th}}$ and $\boldsymbol{\theta_{th}}$ are field and torque thermal noise vectors, respectively. The effective field and torque are derived from the Helmholtz free energy (equations (3) and (4) without $\boldsymbol{H_{app}}$) [26]. The $\boldsymbol{H_{app}}$ represents the additional external field applied to the system, primarily serving as the time-dependent AC and one-dimensional spatial-dependent gradient field in this study. While particle acceleration effects could be incorporated into the effective torque equation, they are neglected here due to the overwhelming influence of viscous forces. It is reasonable to assume that the torque and thermal noise follow a Gaussian distribution.

The torque and field thermal noises are assumed as Gaussian noise in our simulation, with the following correlations:

$$\boldsymbol{\theta}^i_{\boldsymbol{th}}(t)\,\boldsymbol{\theta}^j_{\boldsymbol{th}}(t') = 12k_B T\eta V_h \delta_{ij}\delta(t-t') \tag{5}$$

$$\boldsymbol{H}_{\boldsymbol{th}}{}^i(t)\,\boldsymbol{H}^j_{\boldsymbol{th}}(t') = \frac{2k_B T}{\gamma\mu}\frac{1+\alpha^2}{\alpha}\delta_{ij}\delta(t-t') \tag{6}$$

where k_B is the Boltzmann constant, T is temperature, and δ_{ij} and $\delta(t-t')$ are Kronecker and Dirac delta functions, respectively.

To be more explicit for the Néel attempting time, Brownian relaxation time, and their effects on the magnetization dynamics and the test parameters, equations (1) and (2) can be rewritten as:

$$\frac{d\boldsymbol{n}}{dt} = \frac{-1}{\tau_B}\left(\sigma(\boldsymbol{m}\cdot\boldsymbol{n})(\boldsymbol{m}\times\boldsymbol{n}) + \widetilde{\boldsymbol{\theta}}_{\boldsymbol{th}}\right)\times\boldsymbol{n} \tag{7}$$

$$\frac{d\boldsymbol{m}}{dt} = \frac{1}{\tau_0}\left(\frac{1}{\alpha}\boldsymbol{\xi} + \boldsymbol{m}\times\boldsymbol{\xi} + \frac{1}{\alpha}\widetilde{\boldsymbol{H}}_{\boldsymbol{th}} + \boldsymbol{m}\times\widetilde{\boldsymbol{H}}_{\boldsymbol{th}}\right)\times\boldsymbol{m} \tag{8}$$

where $\tau_B = \frac{3V_h\eta}{k_B T}$ is the Brownian relaxation time, $\tau_0 = \frac{\mu\left(1+\alpha^2\right)}{2k_B T\alpha\gamma}$ is the Néel attempting time which relates to the commonly known Néel relaxation time, $\sigma = \frac{K_a V_c}{k_B T}$ is the unitless anisotropy energy, and $\boldsymbol{\xi} = \frac{\mu_0\mu\boldsymbol{H_{app}}(z,t)}{2k_B T} + \sigma(\boldsymbol{m}\cdot\boldsymbol{n})\boldsymbol{n}$. μ_0 is the vacuum permeability. In this form, the reduced form of correlations become equal to the Néel attempting and Brownian relaxation time by:

$$\widetilde{\boldsymbol{\theta}}^i_{\boldsymbol{th}}(t)\,\widetilde{\boldsymbol{\theta}}^j_{\boldsymbol{th}}(t') = \tau_B\delta_{ij}\delta(t-t') \tag{9}$$

$$\widetilde{\boldsymbol{H}}^i_{\boldsymbol{th}}(t)\,\widetilde{\boldsymbol{H}}^j_{\boldsymbol{th}}(t') = \tau_0\delta_{ij}\delta(t-t'). \tag{10}$$

We consider the excitation field applied along the Z direction and model the magnetic dynamics of 1000 SPIONs with typical numerical methods for stochastic Langevin equation and Stratonovich interpretation. The averaged dynamic magnetizations of SPIONs along the excitation field direction, M_z, are recorded, a sampling frequency of 25 MHz, and a low-pass filter with a cutoff frequency of 250 kHz and plotted as M–t curves. The dynamic magnetizations vs excitation field (along the Z direction) in one period of the excitation field is plotted as M–H curves.

Based on the M–H curves, the PSFs are plotted. In the Langevin model $M = M_s L(\xi)$, the PSF was defined as the derivative of the magnetization model (i.e. Langevin function $L(\xi)$) by Goodwill *et al* [12]. Similarly, in this work, we derived a vector form of magnetization $\boldsymbol{M} = M_s\boldsymbol{m}(\xi, \tau_0, \tau_B)$ and defined the PSF as $dm/d\xi$ vs ξ' where $\xi' = \frac{\mu_0\mu\boldsymbol{H_{app}}(\boldsymbol{FFR})}{2k_B T}$. This derivative captures the influence of the excitation field, anisotropy field, magnetic moment, Brownian relaxation, and Néel attempt time. Furthermore, we use the FWHM as a parameter to evaluate the intrinsic spatial resolution in MPI systems. It is reported that this resolution, Δx, can be determined by [33]:

$$\Delta x = \frac{k_B T}{\mu_0\mu G}\xi_{\mathrm{FWHM}} \tag{11}$$

where G is the strength of the gradient field and ξ_{FWHM} is the FWHM that can be measured from the PSF. The magnetization analysis over time is influenced by side lobes in the frequency domain, while the analysis over the external fields is impacted by a high magnetization ratio near saturation points. To address these issues, the Kaiser windowing technique followed by a Savitzky–Golay filter is employed.

The parameters and values used in this work are summarized in table 1.

3. Results and discussion

3.1. Effect of magnetic core size on the MPI resolution

The size of the magnetic core is a fundamental physical property of tracers. To achieve a prolonged blood circulation time of SPION tracers for *in vivo* applications such as MPI, particles with core diameters ranging from 10 to 30 nm are preferred [41]. In this section, we first studied the effect of tracers' magnetic core sizes on the MPI performance. Considering that different synthesis methods, oxidation stages, unforeseeable defects in crystalline solids, variations in particle shapes, etc can result in SPIONs with a wide range of saturation magnetization (M_S) and effective magnetic anisotropy (K_a) values, it is reasonable to assume intermediate values for these properties in the modeling. Thus, based on the reported works, we fixed these variables at $M_S = 300$ kA m^{-1} and $K_a = 3$ kJ m^{-3} [42, 43]. For simplicity, a uniaxial anisotropy is assumed for all SPIONs. The non-magnetic coating layer is assumed to be 5 nm thick, and we varied the spherical SPION tracers' core diameter D from 20 to 60 nm. A total of 1000 non-interacting SPOINs are assumed in the FFR. As shown in figure 2(a), when subjected to a Z-direction excitation field of 25 kHz and 20 mT/μ_0, the averaged M–t curves of these SPOINs in an FFR along the field direction (Z axis) are recorded as M_z.

Equations (7) and (8) are used to provide an understanding of the outcomes. When dealing with short-time behavior in the scale of the Winner process, the coefficients of $\frac{1}{\tau_0}$ in equation (8) remain relatively constant while the Néel attempting time is subject to changes over time being shorter

Table 1. Parameters and values in this work.

Variable	Values	References
Viscosity (Pa·s)	0.001	—
Temperature (K)	300	—
Gradient field magnitude (T/m/μ_0)	3	[34–36]
Damping parameter α	1	[26]
Gyromagnetic ratio γ (GHz/T)	176	[37]
Magnetic core diameter D_c (nm)	$D_c = 20, 30, 40, 50, 60$	[38–40]
Hydrodynamic diameter D_h (nm)	$D_h = D_c + 0, D_c + 5,$ $D_c + 10, D_c + 15,$ $D_c + 25, D_c + 30$	
Magnetic anisotropy K_a (kJ m^{-3})	3, 5, 8, 10, 15	
Saturation magnetization M_S (kA m^{-1})	50, 100, 200, 300, 400, 500	
Excitation field amplitude (mT/μ_0)	20	[1, 39]
Excitation field frequency (kHz)	25	

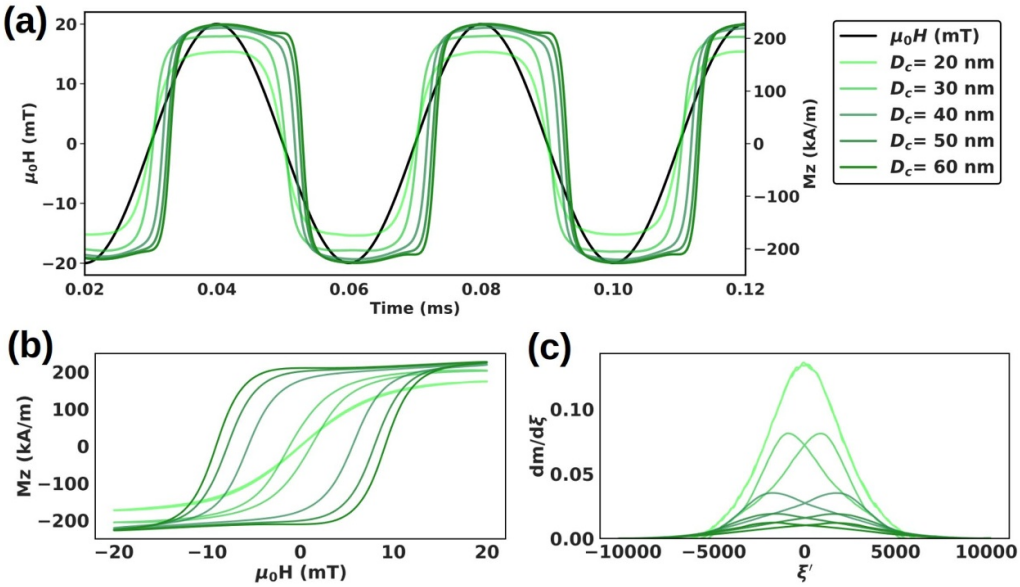

Figure 2. Dynamic magnetization responses of SPIONs with varying magnetic core sizes from 20 nm to 60 nm, subjected to an excitation field of 25 kHz and 20 mT/μ_0. (a) M–t curves. As a reference, the excitation field is also plotted. (b) and (c) are M–H curves and PSF profiles, respectively.

than the random jumps. The fastest timing aspect within the system is determined by the Néel attempting time (see table 2). Consequently, integrating equation (8) shows a pattern in magnetization with its growth influenced by the Néel attempting time and is not significantly influenced by the Brownian dynamics of 1000 SPIONs on average. This polynomial trend leads to distortions in the magnetization response signal compared to the sinusoidal excitation field (as shown in figure 2(a)), causing changes in reaction to variations in field strength (as depicted in figure 2(b)). As the Néel attempting time is linked to core size, an increase in core size results in a decrease in this timing aspect, leading to polynomial variations as the $\frac{1}{\tau_0}$ diminish. Consequently, polynomial changes result in a larger delay experienced by the response, and the M–H curve tends towards a steeper sigmoidal behavior. Therefore, SPIONs with larger core sizes show a steeper transition to the saturation point, which widens the M–H curve (figure 2(b)). However, the larger core size also increases the anisotropy

Table 2. Effect of SPION tracers' magnetic core sizes on Néel attempting time, Brownian relaxation time, and FWHM in PSF profiles.

D_c (nm)	τ_B (μs)	τ_0 (μs)	FWHM[a]
20	1.025	1.725×10^{-3}	4.75
30	2.428	5.821×10^{-3}	4.36
40	4.743	1.380×10^{-2}	5.92
50	8.196	2.695×10^{-2}	7.14
60	130.141	4.657×10^{-2}	7.715

[a] The unit of FWHM can be achieved by ξ'.

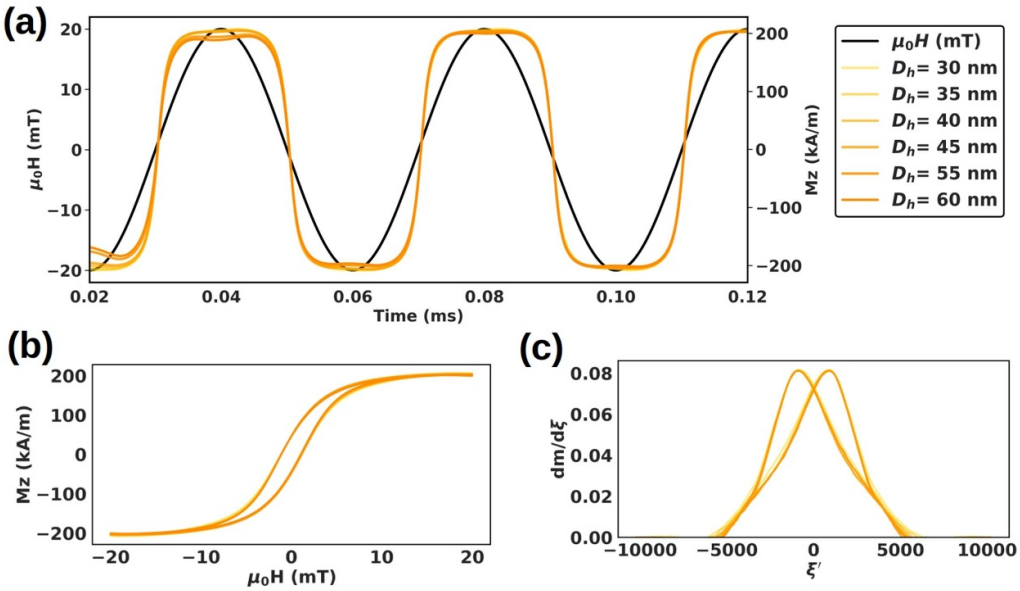

Figure 3. Dynamic magnetization responses of 30 nm core size SPIONs with varying hydrodynamic sizes, subjected to an excitation field of 25 kHz and 20 mT/μ_0. (a)–(c) are the M–t curves, M–H curves, and PSF profiles, respectively.

field. The increased anisotropy field introduces greater distortion in response to the excitation field. This distortion reduces the alignment of the particle response to the excitation field, which results in diminishing the PSF peaks (figure 2(c)). From the PSF profiles of SPIONs, the FWHM is collected and summarized in table 2. The FWHM is smaller for SPIONs with smaller core sizes, suggesting higher MPI spatial resolution can be achieved with smaller tracer core sizes.

3.2. Effect of hydrodynamic size on the MPI resolution

For improved colloidal stability, higher biocompatibility, enhanced internalization in cells, etc, SPION tracers are often surface functionalized with non-magnetic layers such as polymers, small molecules, silica, metal oxides, graphene, etc [44, 45]. With these surface coatings, the hydrodynamic size of SPIONs inevitably increases, which significantly affects their rotational dynamics, particularly concerning the Brownian motions.

Herein, we assumed an ensemble of 1000 non-interacting SPION tracers with fixed $M_S = 300$ kA m^{-1}, $K_a = 3$ kJ m^{-3}, and core diameter $D_c = 30$ nm. We varied the thickness of the surface non-magnetic coating layer at 0 nm ($D_h = 30$ nm), 2.5 nm ($D_h = 35$ nm), 5 nm ($D_h = 40$ nm), 7.5 nm ($D_h = 45$ nm), 12.5 nm ($D_h = 55$ nm), and 15 nm ($D_h = 60$ nm). The varying hydrodynamic sizes directly affect the Brownian relaxation time and the Brownian relaxation dynamics as indicated in equation (7). On the other hand, the identical magnetic core sizes lead to the same τ_0 values in equation (8).

Due to the faster Néel attempting time dominating the magnetization dynamics of SPIONs. Only minor changes in magnetizations and FWHM are expected as illustrated in figures 3(a)–(c) and summarized in table 3. In conclusion, for an ensemble of 30 nm SPIONs, the coating size does not have a significant effect on the dynamic magnetizations of the ensemble on average. However, a thicker coating layer does lead to increased noise in the Brownian dynamics, as can be seen from equations (7)–(9). A thicker coating layer leads to longer Brownian relaxation time, which in turn, increases the Brownian rotation dynamics and noise. This causes more noise to the observed dynamic magnetizations. Nevertheless, averaging over the number of particles and low-pass filter compensates for the overall noise results from the thicker coating.

3.3. Effect of magnetic anisotropy on the MPI resolution

Due to different synthesis methods, varying degrees of oxidation, different levels of crystalline defects, various surface coating materials, and different shapes, even SPIONs with

Table 3. Effect of SPION tracers' surface non-magnetic coating layers on Néel attempting time, Browning relaxation time, and FWHM in PSF profiles.

Non-magnetic Coating Thickness (nm)	τ_B (μs)	τ_0 (μs)	FWHM[a]
0 ($D_h = 30$)	10.244	5.821×10^{-3}	4.68
2.5 ($D_h = 35$)	16.268	5.821×10^{-3}	4.46
5 ($D_h = 40$)	24.283	5.821×10^{-3}	4.39
7.5 ($D_h = 45$)	34.575	5.821×10^{-3}	4.32
12.5 ($D_h = 55$)	63.126	5.821×10^{-3}	4.51
15 ($D_h = 60$)	81.955	5.821×10^{-3}	4.70

[a] The unit of FWHM can be achieved by ξ'.

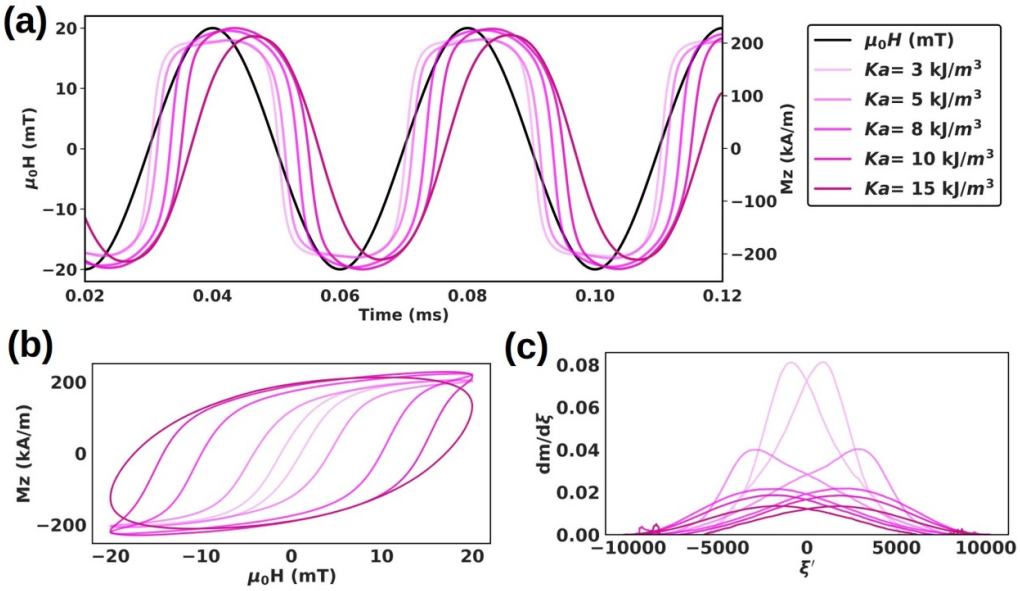

Figure 4. Dynamic magnetization responses of 30 nm core size SPIONs with varying magnetic anisotropy values, subjected to an excitation field of 25 kHz and 20 mT/μ_0. (a)–(c) are the *M*–*t* curves, *M*–*H* curves, and PSF profiles, respectively.

identical core sizes and materials exhibit significant variations in magnetic anisotropy values, as reported in various studies [20, 21, 46]. For iron oxide nanoparticles with magnetic core sizes less than 100 nm, the reported effective magnetic anisotropy typically ranges from 3 to 11 kJ m^{-3} [42].

Herein, for an ensemble of 1000 non-interacting SPIONs, we fixed their $M_S = 300$ kA m^{-1}, core diameter $D_c = 30$ nm, hydrodynamic size $D_h = 40$ nm (a 5 nm thick non-magnetic coating layer is assumed) and varied magnetic anisotropy K_a from 3 to 15 kJ m^{-3}. Subjecting these SPION tracers to the excitation field, figure 4 summarizes the effect of varying magnetic anisotropy values on their dynamic magnetization behaviors. Changes in anisotropy do not affect the Néel attempting time, meaning anisotropy does not affect magnetization dynamics concerning the Néel dynamics (equation (8)). However, anisotropy directly impacts system dynamics through unitless anisotropy energy σ (equation (7)). The anisotropy field aligns with the easy axis direction (second term in ξ) and increases the delay in the MNPs' response to the field as it grows. Consequently, the *M*–*t* curves exhibit greater delays in responding to the excitation field (figure 4(a)), while the *M*–*H* curves become broader (figure 4(b)). With higher anisotropy, the magnetization response becomes significantly distorted, eventually resembling the sinusoidal behavior of the excitation field, but with a delay (figure 4(a)). Furthermore, the larger distortion reduces the PSF peaks (figure 4(c)), like the impact of particle core size, as both the anisotropy constant and core size directly affect the anisotropy field ($\sigma = \frac{K_a V_c}{k_B T}$). As a result, the PSF peaks decrease, and the FWHM increases, as shown in figure 4(c) and summarized in table 4.

Table 4. Effect of SPION tracers' magnetic anisotropy values on Néel attempting time, Brownian relaxation time, anisotropy energy, and FWHM in PSF profiles.

K_a (kJ m^{-3})	σ	τ_B (μs)	τ_0 (μs)	**FWHM**[a]
3	5.928	24.283	3.368×10^{-3}	4.37
5	9.881	24.283	3.368×10^{-3}	6.71
8	15.809	24.283	3.368×10^{-3}	8.96
10	19.761	24.283	3.368×10^{-3}	15.34
15	29.642	24.283	3.368×10^{-3}	—

[a] The unit of FWHM can be achieved by ξ'.

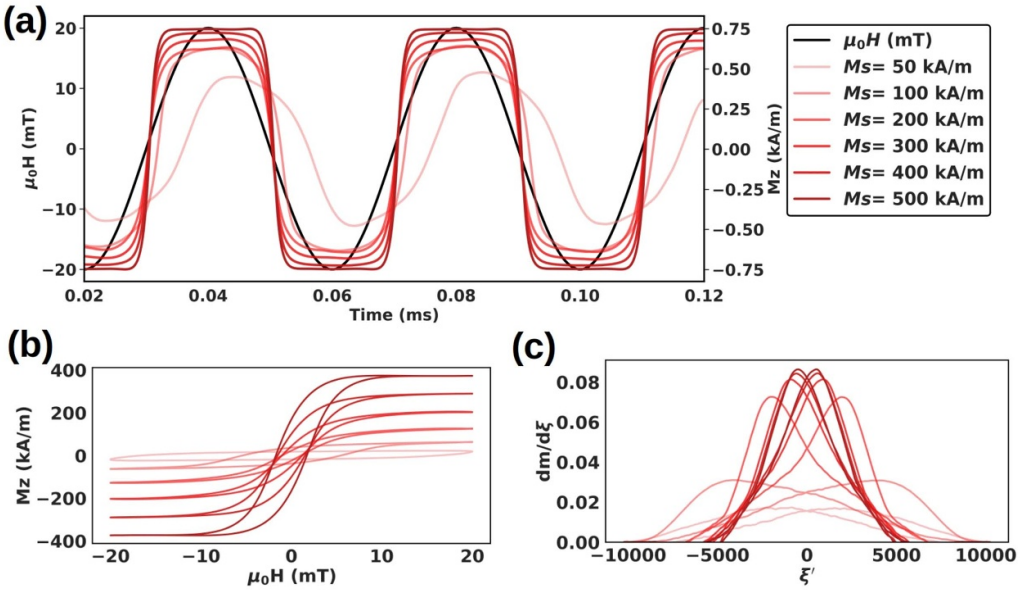

Figure 5. Dynamic magnetization responses of 30 nm core size SPIONs with varying saturation magnetization values, subjected to an excitation field of 25 kHz and 20 mT/μ_0. (a)–(c) are the *M*–*t* curves, *M*–*H* curves, and PSF profiles, respectively.

Table 5. Effect of SPION tracers' saturation magnetization values on Néel attempting time, Brownian relaxation time, and FWHM in PSF profiles.

M_S (kA m^{-1})	τ_B (μs)	τ_0 (μs)	FWHM[a]
50	24.283	9.701×10^{-4}	9.61
100	24.283	1.940×10^{-3}	9.82
200	24.283	3.880×10^{-3}	4.56
300	24.283	5.821×10^{-3}	4.39
400	24.283	7.761×10^{-3}	4.25
500	24.283	9.701×10^{-3}	4.02

[a] The unit of FWHM can be achieved by ξ'.

3.4. Effect of saturation magnetization on the MPI resolution

Like magnetic anisotropy, the saturation magnetization of SPIONs also varies in a wide range due to synthesis methods, degrees of oxidation, and more, but this value of SPIONs is generally lower than the saturation magnetization of iron oxide bulk material, which is 80–100 Am^2 kg^{-1} (equal to 400–525 kA m^{-1} if considering the mass density of 5,250 kg m^{-3}) [47]. Herein, we varied the saturation magnetization values of 1000 non-interacting SPIONs from 50 to 500 kA m, while fixing other values $D_c = 30$ nm, $D_h = 40$ nm, and $K_a = 3$ kJ m^{-3}.

Figure 5(a) shows the *M*–*t* curves of SPOINs with varying saturation magnetization values. For a core size of 30 nm and small anisotropy of 3 kJ m^{-3}, all SPIONs can reach saturation under a 20 mT/μ_0 and 25 kHz excitation field. Due to this fact, the different saturation values only show a direct impact on the slew rate of magnetizations in the *M*–*H* curves in figure 5(b). This varying slew rate, as a result, leads to different FWHM in the PSF profiles (see figure 5(c) and table 5). In summary, a higher saturation magnetization leads to improved MPI spatial resolution.

4. Conclusions

The design of SPION tracers tailored for MPI applications holds an important role in improving the intrinsic spatial resolution. Currently, most of the MPI works use SPIONs and other magnetic nanoparticles that are designed for magnetic resonance imaging. However, these tracers are usually not suitable for MPI. Herein, we applied a stochastic Langevin function with coupled Brownian–Néel relaxation models to simulate the dynamic magnetization responses of SPION tracers in MPI application. An ensemble of 1000 non-interacting SPION tracers is assumed in the FFR and subjected to an excitation field of 25 kHz and 20 mT/μ_0. Their *M*–*t* curves, *M*–*H* curves, and PSF profiles are collected to evaluate their performance in MPI imaging applications.

In our models, we varied some important physical and magnetic properties of tracers, such as magnetic core size in section 3.1, hydrodynamic size (i.e. surface non-magnetic coating layer) in section 3.2, magnetic anisotropy in section 3.3, and saturation magnetization in section 3.4. When studying the effect of one parameter, the other material parameters are fixed. Our results indicate that a higher MPI spatial resolution can be achieved with higher saturation magnetizations of tracers. While the surface coating layers on SPION tracers can introduce higher noise in the magnetization dynamics, they do not significantly impact the magnetization dynamics or MPI spatial resolution, as the faster Néel attempting time dominates the dynamic magnetization responses of the modeled SPIONs. As magnetic anisotropy values and core sizes increase, the dominant relaxation mechanism shifts from Néel to Brownian, leading to a complex rise and fall in dynamic magnetizations, which may affect the SNR of the MPI signal. Our conclusion is based on the assumption that the intrinsic spatial resolution of MPI is positively proportional to FWHM and negatively proportional to

the gradient field strength G (T/m/μ_0) [29, 33]. It should also be noted that the FWHM from PSF is only one of the several factors that intrinsically affect the imaging spatial resolution of MPI. Other factors such as the temperature, receive coil sensitivity, SNR of the circuit for signal post-processing (i.e. amplification, filtering, analog-to-digital convert, etc), image reconstruction algorithm, etc, can also affect the MPI imaging resolution.

Although this study shows the effects of several factors in MPI imaging, these parameters are not fully optimized due to the following limitations. The stochastic Langevin model's computational complexity demands significant processing power to simulate realistic scenarios, especially when dealing with high or varied particle concentrations. Combinatorial adjustment of parameters, such as core size, anisotropy, and saturation magnetization, allows for experimental design refinement and better validation of the model for parameter optimization. Enhancing and testing the stochastic Langevin function experimentally can also improve its capacity to account for internal particle interactions, dynamic behaviors, and their effects on the MPI image resolution.

Data availability statement

Codes used in this work are available at: https://github.com/AbrahamAzizi/MPI-StochasticLangevinModel/tree/main/MNP-properties.

Acknowledgments

K W acknowledges the financial support by Texas Tech University through HEF New Faculty Startup, NRUF Start Up, and Core Research Support Fund. B R acknowledges the Distinguished Graduate Student Assistantships (DGSA) offered by Texas Tech University.

Conflict of interest

The author declares no conflict of interest.

ORCID iDs

Ebrahim Azizi https://orcid.org/0000-0002-0230-2534
Shahriar Mostufa https://orcid.org/0000-0002-3326-4817
Bahareh Rezaei https://orcid.org/0000-0003-3446-3559
Shumin Xin https://orcid.org/0009-0000-3082-6434
Jiajia Sun https://orcid.org/0009-0006-7670-3396
Zongqian Shi https://orcid.org/0000-0003-3347-2058
Jenifer Gómez-Pastora https://orcid.org/0000-0002-5157-4130
Kai Wu https://orcid.org/0000-0002-9444-6112

References

[1] Knopp T and Buzug T M 2012 *Magnetic Particle Imaging: An Introduction to Imaging Principles and Scanner Instrumentation* (Springer Science & Business Media)
[2] Rezaei B *et al* 2024 Magnetic nanoparticles for magnetic particle imaging (MPI): design and applications *Nanoscale* **16** 11802–24
[3] Gleich B and Weizenecker J 2005 Tomographic imaging using the nonlinear response of magnetic particles *Nature* **435** 1214–7
[4] Zhou X Y, Tay Z W, Chandrasekharan P, Elaine Y Y, Hensley D W, Orendorff R, Jeffris K E, Mai D, Zheng B and Goodwill P W 2018 Magnetic particle imaging for radiation-free, sensitive and high-contrast vascular imaging and cell tracking *Curr. Opin. Chem. Biol.* **45** 131–8
[5] Meola A, Rao J, Chaudhary N, Song G, Zheng X and Chang S D 2019 Magnetic particle imaging in neurosurgery *World Neurosurg.* **125** 261–70
[6] Gräser M, Thieben F, Szwargulski P, Werner F, Gdaniec N, Boberg M, Griese F, Möddel M, Ludewig P and van de Ven D 2019 Human-sized magnetic particle imaging for brain applications *Nat. Commun.* **10** 1–9
[7] Yu E Y, Chandrasekharan P, Berzon R, Tay Z W, Zhou X Y, Khandhar A P, Ferguson R M, Kemp S J, Zheng B and Goodwill P W 2017 Magnetic particle imaging for highly sensitive, quantitative, and safe *in vivo* gut bleed detection in a murine model *ACS Nano* **11** 12067–76
[8] Yoshida T and Enpuku K 2024 Field-dependent Néel relaxation time of magnetic nanoparticles in AC excitation fields: boundary field between Néel- and Brownian-dominant regions *J. Appl. Phys.* **135** 093901
[9] Feng X *et al* 2023 Relaxation spectral analysis in multi-contrast vascular magnetic particle imaging *Med. Phys.* **50** 4651–63
[10] Knopp T, Rahmer J, Sattel T F, Biederer S, Weizenecker J, Gleich B, Borgert J and Buzug T M 2010 Weighted iterative reconstruction for magnetic particle imaging *Phys. Med. Biol.* **55** 1577–89
[11] Knopp T, Sattel T F, Biederer S, Rahmer J, Weizenecker J, Gleich B, Borgert J and Buzug T M 2010 Model-based reconstruction for magnetic particle imaging *IEEE Trans. Med. Imaging* **29** 12–18
[12] Goodwill P W and Conolly S M 2010 The X-space formulation of the magnetic particle imaging process: 1-D signal, resolution, bandwidth, SNR, SAR, and magnetostimulation *IEEE Trans. Med. Imaging* **29** 1851–9
[13] Goodwill P W and Conolly S M 2011 Multidimensional x-space magnetic particle imaging *IEEE Trans. Med. Imaging* **30** 1581–90
[14] Goodwill P W, Lu K, Zheng B and Conolly S M 2012 An x-space magnetic particle imaging scanner *Rev. Sci. Instrum.* **83** 033708
[15] Tay Z W, Hensley D W, Vreeland E C, Zheng B and Conolly S M 2017 The relaxation wall: experimental limits to improving MPI spatial resolution by increasing nanoparticle core size *Biomed. Phys. Eng. Express* **3** 035003
[16] Bauer L M, Situ S F, Griswold M A and Samia A C S 2015 Magnetic particle imaging tracers: state-of-the-art and future directions *J. Phys. Chem. Lett.* **6** 2509–17
[17] Albers H, Thieben F, Boberg M, Scheffler K, Knopp T and Kluth T 2023 Model-based calibration and image reconstruction with immobilized nanoparticles *Int. J. Magn. Part. Imaging* IJMPI **9** 2303002
[18] Kluth T, Szwargulski P and Knopp T 2019 Towards accurate modeling of the multidimensional magnetic particle imaging physics *New J. Phys.* **21** 103032

[19] Li Y, Hui H, Zhang P, Zhong J, Yin L, Zhang H, Zhang B, An Y and Tian J 2023 Modified Jiles–Atherton model for dynamic magnetization in X-space magnetic particle imaging *IEEE Trans. Biomed. Eng.* **70** 2035–45
[20] Yari P, Chugh V K, Saha R, Tonini D, Rezaei B, Mostufa S, Xu K, Wang J-P and Wu K 2023 Static and dynamic magnetization models of magnetic nanoparticles: an appraisal *Phys. Scr.* **98** 082002
[21] Wu K, Su D, Saha R, Wong D and Wang J-P 2019 Magnetic particle spectroscopy-based bioassays: methods, applications, advances, and future opportunities *J. Phys. Appl. Phys.* **52** 173001
[22] Shasha C and Krishnan K M 2021 Nonequilibrium dynamics of magnetic nanoparticles with applications in biomedicine *Adv. Mater.* **33** 1904131
[23] Wu K, Schliep K, Zhang X, Liu J, Ma B and Wang J 2017 Characterizing physical properties of superparamagnetic nanoparticles in liquid phase using Brownian relaxation *Small* **13** 1604135
[24] Shah S A, Reeves D B, Ferguson R M, Weaver J B and Krishnan K M 2015 Mixed Brownian alignment and Néel rotations in superparamagnetic iron oxide nanoparticle suspensions driven by an ac field *Phys. Rev.* B **92** 094438
[25] Usov N and Liubimov B Y 2012 Dynamics of magnetic nanoparticle in a viscous liquid: application to magnetic nanoparticle hyperthermia *J. Appl. Phys.* **112** 023901
[26] Reeves D B and Weaver J B 2015 Combined Néel and Brown rotational Langevin dynamics in magnetic particle imaging, sensing, and therapy *Appl. Phys. Lett.* **107** 223106
[27] Reeves D B and Weaver J B 2012 Simulations of magnetic nanoparticle Brownian motion *J. Appl. Phys.* **112** 124311
[28] Weizenecker J 2018 The Fokker–Planck equation for coupled brown–Néel-rotation *Phys. Med. Biol.* **63** 035004
[29] Jiang T, Yi W, Du Z and Liu W 2022 An improved point spread function for complex susceptibility-based magnetic particle imaging *Meas. Sci. Technol.* **33** 095402
[30] Bagheri H and Hayden M E 2020 Resolution enhancement in magnetic particle imaging via phase-weighting *J. Magn. Magn. Mater.* **498** 166021
[31] Croft L R, Goodwill P W, Konkle J J, Arami H, Price D A, Li A X, Saritas E U and Conolly S M 2015 Low drive field amplitude for improved image resolution in magnetic particle imaging: low drive field amplitude for improved image resolution *Med. Phys.* **43** 424–35
[32] Murase K 2020 Simultaneous correction of sensitivity and spatial resolution in projection-based magnetic particle imaging *Med. Phys.* **47** 1845–59
[33] Rahmer J, Weizenecker J, Gleich B and Borgert J 2009 Signal encoding in magnetic particle imaging: properties of the system function *BMC Med. Imaging* **9** 1–21
[34] Tay Z W, Hensley D W, Chandrasekharan P, Zheng B and Conolly S M 2020 Optimization of drive parameters for resolution, sensitivity and safety in magnetic particle imaging *IEEE Trans. Med. Imaging* **39** 1724–34
[35] Goodwill P W, Konkle J J, Zheng B, Saritas E U and Conolly S M 2012 Projection x-space magnetic particle imaging *IEEE Trans. Med. Imaging* **31** 1076–85
[36] Vogel P, Rückert M A, Klauer P, Kullmann W H, Jakob P M and Behr V C 2013 Traveling wave magnetic particle imaging *IEEE Trans. Med. Imaging* **33** 400–7
[37] Kluth T 2018 Mathematical models for magnetic particle imaging *Inverse Problems* **34** 083001
[38] Wu K, Su D, Liu J, Saha R and Wang J-P 2019 Magnetic nanoparticles in nanomedicine: a review of recent advances *Nanotechnology* **30** 502003
[39] Wu K *et al* 2024 Roadmap on magnetic nanoparticles in nanomedicine *Nanotechnology* **36** 042003
[40] Wu K, Liu J, Chugh V K, Liang S, Saha R, Krishna V D, Cheeran M C and Wang J-P 2022 Magnetic nanoparticles and magnetic particle spectroscopy-based bioassays: a 15-year recap *Nano Futures* 6 022001
[41] Akbarzadeh A, Samiei M and Davaran S 2012 Magnetic nanoparticles: preparation, physical properties, and applications in biomedicine *Nanoscale Res. Lett.* **7** 144
[42] Ludwig F, Remmer H, Kuhlmann C, Wawrzik T, Arami H, Ferguson R M and Krishnan K M 2014 Self-consistent magnetic properties of magnetite tracers optimized for magnetic particle imaging measured by ac susceptometry, magnetorelaxometry and magnetic particle spectroscopy *J. Magn. Magn. Mater.* **360** 169–73
[43] Shasha C, Teeman E and Krishnan K M 2017 Harmonic simulation study of simultaneous nanoparticle size and viscosity differentiation *IEEE Magn. Lett.* **8** 1–5
[44] Villanueva A, Canete M, Roca A G, Calero M, Veintemillas-Verdaguer S, Serna C J, Del Puerto Morales M and Miranda R 2009 The influence of surface functionalization on the enhanced internalization of magnetic nanoparticles in cancer cells *Nanotechnology* **20** 115103
[45] Rezaei B, Yari P, Sanders S M, Wang H, Chugh V K, Liang S, Mostufa S, Xu K, Wang J-P and Gómez-Pastora J 2023 Magnetic nanoparticles: a review on synthesis, characterization, functionalization, and biomedical applications *Small* **20** 2304848
[46] Greculeasa S G, Palade P, Schinteie G, Leca A, Dumitrache F, Lungu I, Prodan G, Kuncser A and Kuncser V 2020 Tuning structural and magnetic properties of Fe oxide nanoparticles by specific hydrogenation treatments *Sci. Rep.* **10** 17174
[47] Cornell R M and Schwertmann U 2003 *The Iron Oxides: Structure, Properties, Reactions, Occurrences, and Uses* vol 664 (Wiley)